CrossMark

Minute-timescale Variability in the X-ray Emission of the Highest Redshift Blazar[*]

Alberto Moretti[1] , Gabriele Ghisellini[2] , Alessandro Caccianiga[1] , Silvia Belladitta[1,3] , Roberto Della Ceca[1] ,
Luca Ighina[1,3], Tullia Sbarrato[2] , Paola Severgnini[1] , and Cristiana Spingola[4]

[1] INAF, Osservatorio Astronomico di Brera Via Brera 28 I-20121 Milano, Italy; alberto.moretti@inaf.it
[2] INAF, Osservatorio Astronomico di Brera Via E. Bianchi 46 I-23807 Merate (LC), Italy
[3] DiSAT, Università degli Studi dell'Insubria Via Valleggio 11 I-22100 Como, Italy
[4] INAF, Istituto di Radioastronomia Via Gobetti 101 I-40129 Bologna, Italy

Abstract

We report on two Chandra observations of the quasar PSO J0309+27, the most distant blazar observed so far ($z = 6.1$), performed eight months apart, in 2020 March and November. Previous Swift-XRT observations showed that this object is one of the brightest X-ray sources beyond redshift 6.0 ever observed so far. This new dataset confirmed the high flux level and unveiled a spectral change that occurred on a very short timescale (250 s rest frame), caused by a significant softening of the emission spectrum. This kind of spectral variability, on such a short interval, has never been reported in the X-ray emission of a flat-spectrum radio quasar. A possible explanation for this is given by the emission produced by the inverse Compton scatter of the quasar UV photons by the cold electrons present in a fast shell moving along the jet. Although this bulk Comptonization emission should be an unavoidable consequence of the standard leptonic jet model, this would be the first time that it has been observed.

Unified Astronomy Thesaurus concepts: Blazars (164); Flat-spectrum radio quasars (2163); Radio loud quasars (1349); Jets (870); Quasars (1319)

1. Introduction

Radio-loud quasars (RL QSOs) are characterized by the presence of relativistic jets, huge collimated outflows originating very close to the accreting supermassive black hole (SMBH) and extending up to extragalactic distances (Harris & Krawczynski 2006; Blandford et al. 2019). When aligned with our line of sight, the jet overwhelms most of the emission from the other nuclear components. In this case, RL QSOs are called blazars and their typical spectral energy distribution shows two main peaks, the first falling between the IR and the X-ray energy bands and the second at gamma-ray frequencies (see Madejski & Sikora 2016, for a recent review). According to the standard picture, the low-energy component is synchrotron radiation produced by a population of electrons moving at highly relativistic velocities in random directions within the jet flow. The high-energy photons are thought to be produced by the so-called self-synchrotron Compton (SSC) mechanism, which is the inverse Compton (IC) scatter of the same electrons on the low-energy photons produced via the synchrotron mechanism (Sikora et al. 1997; Ghisellini & Tavecchio 2009, e.g.). Flat-spectrum radio quasars (FSRQ), which are the blazars hosted by QSOs, are characterized by a dense, radiative, circumnuclear environment. In these cases, other possible IC seed photons can be external to the jet, like the ones produced in the accretion disk (AD) and reprocessed by broad-line regions (BLR) or by the dusty torus. On a larger scale, stellar radiation of the host galaxy and the cosmic microwave background photons on the extragalactic scale are expected to contribute (Tavecchio et al. 2000; Harris & Krawczynski 2006).

While multi-wavelength observations generated a broad consensus in the literature on the main emission mechanisms, there are some fundamental aspects of the jet nature that still escape understanding. One of the most basic issues is their

composition: a large amount of energy is observed moving through the jet from the very central part of the QSO up to the megaparsec scale. Energy can be transported by a combination of leptons, protons, and Poynting flux. It is not clear what the relative contribution of the different elements is and how it depends on the distance from the SMBH (Sikora et al. 2005). Determining the composition would allow us to calculate the jet total power and to assess its impact on the QSO environment. Moreover, knowing the baryon and lepton loads of the jets would be useful to ascertain their formation mechanism (Sikora & Madejski 2000). The investigation of the spectral variability is a very effective tool with which to probe the properties and the dynamics of the radiating particles and to gain some insight on the physical processes responsible for the observed emission.

In this paper we report on the Chandra observation of PSO J030947.49+271757.31, hereafter PSO J0309+27, the most powerful radio-loud QSO at redshift higher than 6 ($z = 6.1$). The original aim of the Chandra observation was to ascertain the presence and the characteristics of the jet emission. The imaging data analysis together with the properties of the kpc-scale X-ray emission will be presented in a forthcoming paper (L. Ighina et al. 2021, in preparation). Here we focus on the core emission in which we detected a significant spectral variation on the surprisingly short observed timescale of ∼2 ks. While other convincing explanations are lacking in the literature, these data are close to what had been predicted in a scenario of bulk comptonization (BC). In Section 2 we briefly describe the multi-wavelength database currently available for the source. In Section 3 we present the Chandra data timing and spectral analysis. In Section 4 we discuss the interpretation of this observation as due to the BC of UV photons of the QSO by the cold electrons of the jet.

Throughout this paper, errors are quoted at 68% confidence level, unless otherwise specified. We adopt the following cosmology parameter values: $\Omega_m = 0.3$, $\Omega_\Lambda = 0.7$, $h_0 = 0.7$.

---

[*] ...

Table 1
Epoch, Chandra Archive ID, Starting Date, and Duration of the Chandra
Observations of PSO J0309+27

Epoch	Obs Id.	Date	Exp[s]
March	23107	2020-03-24T20:35:21	26,703
November	24513	2020-11-03T10:02:02	19,643
	24855	2020-11-04T00:31:18	8,648
	23830	2020-11-05T14:30:34	21,794
	24856	2020-11-06T11:46:48	23,414
	24512	2020-11-07T14:30:30	27,713

Note. Note that the November observation has been split into 5 different segments.

2. PSO J0309+27

PSO J0309+27 was selected by combining the NRAO VLA Sky Survey, NVSS, and the Panoramic Pan-STARRS catalogs and spectroscopically confirmed as a $z = 6.1$ QSO using the Large Binocular Telescope (LBT) in 2019 October (Belladitta et al. 2020). At $z > 6$ this is by far the most luminous QSO in the radio band.

A relatively short (19 ks) Swift observation, performed between 2019 October and November, detected the source with a flux of $\sim 3.4 \times 10^{-14}$ erg s^{-1} cm^{-2} in the 0.5–10.0 energy band, corresponding to a luminosity of $\sim 10^{45}$ erg s^{-1} in the 2–10 keV band. This allowed us to determine that the X-ray emission is well above the expected coronal emission and it is, with high probability, due to a jet pointing in our direction (Belladitta et al. 2020).

PSO J0309+27 has been observed at the 1.5, 5, and 8.4 GHz frequencies with VLBA in 2020 April under a DDT project (Spingola et al. 2020). The milliarcsecond angular resolution revealed a 500 pc one-sided bright jet resolved into several components. In combination with the core-dominance value (Giovannini et al. 1994), these data constrain the jet Lorentz factor between 3–5 at small viewing angles ($\theta_{view} < 10°$).

PSO J309+27 has been also observed in the near-IR with the LBT-LUCI spectrograph. From this observation, S. Belladitta et al. (2021, in preparation) measure a mass of $8^{+3}_{-2} \times 10^8 M_\odot$ corresponding to a gravitational radius of $\sim 1.2 \times 10^{14}$ cm and a 135 nm luminosity of $1.1 \pm 0.2 \times 10^{46}$ erg s^{-1}, corresponding to a BLR radius of $\sim 2 \times 10^{17}$ cm (Lira et al. 2018). The estimated Eddington ratio is ~ 0.3.

3. Observation and Data Reduction

The first Chandra observation of PSO J0309+27 was performed under Directory Discretionary Time (DDT 704032) on 2020 March 24 for a total effective time of 26.7 ks (Archive Sequence No. 704032, PI: A. Moretti). Then, a 100 ks observation was approved as part of cycle 22. Data were collected in 5 different exposures between 2020 November 3 and November 7 (Table 1) for a total effective time of 101.2 ks (Archive Sequence No. 704242, PI: A. Moretti). Both observations were conducted with the ACIS-S3 detector (CCD = 7) set to very faint mode in order to reduce the background. No data loss occured due to soft proton flares. We reprocessed the data by using the chandra_repro script in CIAO 4.12.1 (Fruscione et al. 2006) and using the CALDB 4.9.3 calibration library.
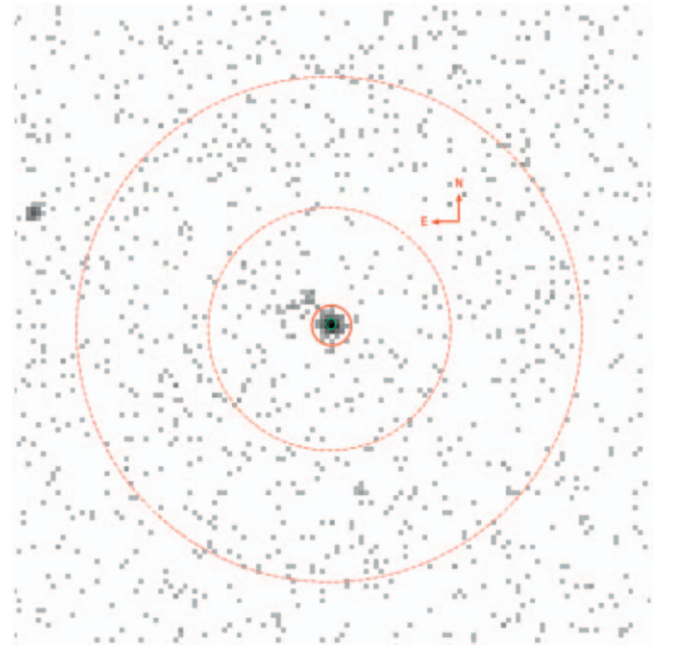

Figure 1. Chandra image of PSO J0309+27. The small red circle and red dashed annuli show the source and background-extraction regions (2″, 12″, 25″ radii, respectively) used for temporal and spectral analysis. The green circle draws the position of the PS1 optical counterpart. An extended emission is clearly visible on the NE direction from the core: its properties will be presented in a forthcoming paper.

The source is detected with 418 photons included in a 1.″5 radius in the 0.5–7.0 keV energy band, with 1.9 background events expected. This makes the background negligible for the purposes of the following analysis.

3.1. Spectral Analysis of the Two Observations

In both the March and November observations, the source spectrum was extracted by means of the specextract CIAO task, using a circular region with a 2″ radius centered on the position as measured by the wavedetect tool. Auxiliary response (ARF) and response matrix (RMF) files have been produced by the same task. The background was estimated in an annulus centered in the same position with 12″ and 25″ as internal and external radii (Figure 1).

Data were fitted in XSPEC (version 12.10.1) using the C-statistics with a simple absorbed power law with the absorption factor fixed to the Galactic value (1.16×10^{21} cm^{-2}) as measured by the HI Galaxy map (Kalberla et al. 2005). The photon index shows a significant variation from $\Gamma = 2.10 \pm 0.20$ in the first observation (March) to $\Gamma = 1.63 \pm 0.10$ in the second (November). This latter value is in agreement with a previous Swift observation (Belladitta et al. 2020) and consistent with the typical FSRQ values, for which an X-ray photon index of $\lesssim 1.8$ is expected (Ighina et al. 2019); by contrast, the spectrum observed in March is significantly softer. The observed flux in the 0.5–10.0 band did not significantly change between the two epochs (Table 2).

To measure the goodness of fit we followed the approach of Medvedev et al. (2021) using the Anderson–Darling test statistic (XSPEC manual).[5] By means of the XSPEC goodness task (with "nosim" and "fit" options) we re-sampled both

---
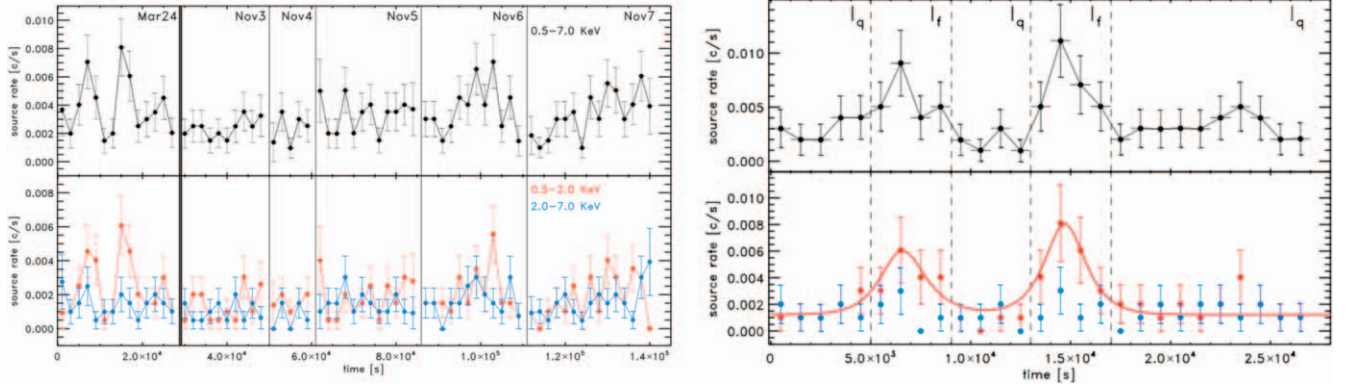[5] https://heasarc.gsfc.nasa.gov/xanadu/xspec/manual

Figure 2. Left panel: background-subtracted light curve of the whole observation with a 2 ks bin. The bars are Poisson error as calculated by the `dmextract` task. For the sake of clarity, bin times are represented in a continuous way, although data have been collected in 6 different and unconnected intervals. The first observation is kept apart by a double continuous line, while the segments of the second observation are divided by dashed lines. Data sets are labeled in accordance with Table 1. The total band data are shown in the upper panel and hard and soft bands in the lower panel in blue and red, respectively. Right panel: light curve of the first observation only in temporal bins of 1 ks. The continuous red line shows the fit to the flares according to the model described in the text. Dashed vertical black lines show the flaring intervals used for the time-resolved spectroscopy.

Table 2
Results of the Spectral Analysis

Epoch	Ph. Index	Flux$_{0.5-2\,keV}$ 10^{-14}erg s^{-1}cm^{-2}	Flux$_{2-10\,keV}$ 10^{-14}erg s^{-1}cm^{-2}	Lum$_{2-10\,keV}$ 10^{45}erg s^{-1}	Lum$_{15-50\,keV}$ 10^{45}erg s^{-1}	dof/cstat (goodness)
(i)	(ii)	(iii)	(iv)	(v)	(vi)	(vii)
Mar	$2.11^{+0.20}_{-0.20}$	$3.23^{+0.47}_{-0.52}$	$3.18^{+0.46}_{-0.51}$	$16.78^{+2.43}_{-2.73}$	$14.65^{+2.12}_{-2.38}$	77/67.21 (74%)
Nov	$1.66^{+0.11}_{-0.11}$	$1.98^{+0.186}_{-0.20}$	$3.86^{+0.36}_{-0.39}$	$8.46^{+0.79}_{-0.85}$	$15.10^{+1.42}_{-1.53}$	176/128.81 (92%)
I$_q$	$1.71^{+0.27}_{-0.26}$	$1.83^{+0.39}_{-0.46}$	$3.30^{+0.70}_{-0.83}$	$7.99^{+1.71}_{-2.00}$	$3.25^{+2.82}_{-3.32}$	44/37.62 (54%)
I$_f$	$2.57^{+0.30}_{-0.30}$	$6.97^{+0.13}_{-0.15}$	$3.47^{+0.65}_{-0.75}$	$44.34^{+8.36}_{-9.63}$	$18.78^{+3.54}_{-4.08}$	43/41.98 (47%)

Note. Single power-law best-fit values of the following data sets are reported: March observation (26.7 ks), November observation (101.7 ks), March quiescent intervals (I$_q$, 18.7 ks), and March flare intervals (I$_f$, 7.9 ks). For each dataset we report: (ii) the photon index, two-band fluxes (iii–iv), and luminosities (v–vi), corrected accounting for the Galactic absorption.

the March and November best-fit models 10,000 times. We found that 74% and 92% of the simulated data sets have better test statistics, respectively. Since the goodness-of-fit tests only allow us to reject a model, this means that a power law is consistent with both data sets.

3.2. Temporal Analysis

To better investigate the spectral variation between the two observations, we used the `dmextract` task to produce the light curve in a temporal bin of 2000 seconds in three different energy bands: wide (0.5–7.0 keV), soft (0.5–2.0 keV), and hard (2.0–7.0 keV). The source and background data were extracted from the same extraction regions used in the spectral analysis. As shown in Figure 2, which shows the background-subtracted, wide-band light curve during the March observation, two intervals of approximately 4000 s each (between 5–9 ks and 13–17 ks from the observation start) present a flux level which is higher with respect to the rest of the observation. As is clear from the comparison between soft- and hard-band curves, this "flaring activity" is almost entirely restricted to energy below 2.0 keV.

To give a first non-parametric estimate of the statistical significance of the observed variation, we made use of a two-dimensional Kolmogorov–Smirnoff test (KS2D, Press et al. 2002, and references therein). We compared the photon-observed inter-arrival time and energy distributions with synthetic samples

generated from non-variable models. For the inter-arrival times Δt we used the exponential distribution $e^{-cr\Delta t}$, where cr is the mean observed count rate, as expected in a Poisson process (Feigelson & Babu 2013). For the energy distribution we used the simple power-law model giving the best fit to the whole dataset 2. We found that 2% of the 10,000 synthetic dataset exceed the distance of our observation from the model. This gives a non-parametric statistical significance of 98% to the observed variability.

In order to give a rough estimate of the characteristic observed variability timescale, we qualitatively modeled the 1 ks binned soft light curve with the following simple analytical function (Hayashida et al. 2015, and references therein)

$$F(t) \propto \frac{1}{e^{-(t-t_0)/\tau_{\rm rise}} + e^{-(t-t_0)/\tau_{\rm fall}}}. \quad (1)$$

We found that the rising and falling parts ($\tau_{\rm raise}$ and $\tau_{\rm fall}$) are ~900 s, as shown in the bottom right panel of Figure 2.

In the following we focus on the time-resolved spectral analysis of the first observation: as we will see, the difference in photon index between the two epochs is entirely restricted to these two episodes.

3.3. Time-resolved Spectral Analysis

In order to characterize the spectral changes, first, we analyzed the March observation data accumulated during the
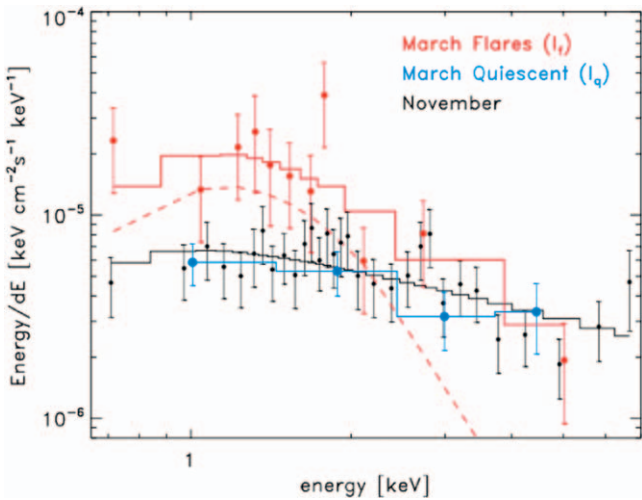
Figure 3. The unfolded spectrum extracted in the I_f, I_q intervals of the March and November observations. Spectral data are plotted as points with vertical error bars. Best-fit models are plotted with continuous lines. Red and blue points show flaring (I_f) and quiet (I_q) intervals, respectively. The latter have been modeled by a simple power law (continuous line). I_f have been fitted by the sum of the I_q power law plus a thermal component shown by the red dashed line. November data, in black, are consistent with I_q data. Data are binned at 2σ significance only for graphical purposes.

flares and during the quiescent periods separately. We considered as flaring the intervals 5095–9127 s and 13095–17127 s from the beginning of the observation (which took place at 701470232.65 satellite time), corresponding to an exposure time of 7959 s. For the seek of simplicity hereafter we will refer to the quiescent and flaring intervals as I_q and I_f, respectively (Figure 2). Using the KS test, we found that the photon energy distribution observed in the I_f interval is different from the rest of the observation, with a confidence of 99.35% (KS probability = 0.0065).

Both I_q and I_f data can be well fitted by single power-law models. The best-fit slope value for I_q is $1.70^{+0.27}_{-0.26}$, closer to and consistent with the second epoch (November) values. I_f data are significantly softer with a photon index best value of $2.58^{+0.30}_{-0.30}$. Using the method described in Section 3.1 we reject the possibility that the two data sets are consistent with a confidence level >99.99%. Indeed, assessing the goodness of fit by the same single power law, we found that 100% out of the 10,000 simulated data sets have better statistics. Source flux in the 0.5–10 keV band doubles during the flaring phase, going from $5.01^{+0.93}_{-0.66} \times 10^{-14}$ erg s^{-1} cm^{-2} during I_q up to $1.05^{+0.16}_{-0.14} \times 10^{-13}$ erg s^{-1} cm^{-2} during the I_f, while the luminosity in the 2.0–10 keV band (0.3–1.4 rest frame) increased by a factor of 5.5. Rather than with a change in the total power-law slope, the same data can be interpreted as due to a transient soft emission. Aiming at testing the BC emission hypothesis, we assumed that the I_f is the sum of the quiescent component observed in I_q plus an extra component, which we modeled as a blackbody (BB) as expected in such a scenario (Celotti et al. 2007). We fit the I_f data as the sum of a power law and a BB, freezing the power-law parameters to the to the I_q best-fit values (Figure 3). The BB model KT best-fit value is $0.33^{+0.07}_{-0.06}$ keV, corresponding to a rest-frame value of $2.34^{+0.50}_{-0.43}$ keV, consistently with that expected from BC scattering of cold jet electrons onto Lyα photons. Flux and luminosity measures are reported in Table 3.

We estimated the goodness of fit following the same procedure described in the previous section for both models,

Table 3
Result of the Spectral Fit to the Transient Component When I_f Data are Fitted by the Sum of a BB and Power Law with Parameters Frozen to the I_q Values

KT KeV (i)	Flux$_{0.5-2\ \mathrm{keV}}$ 10^{-14}erg s^{-1}cm^{-2} (ii)	Lum$_{2-10\ \mathrm{keV}}$ 10^{45}erg s^{-1} (iii)	C-stat/dof (good.) (iv)
$2.39^{+0.53}_{-0.45}$	$3.32^{+0.93}_{-0.76}$	$11.67^{+3.14}_{-2.75}$	41.53/43 (17%)

Note. We list: (i) the BB mean temperature, (ii) flux, and (iv) luminosities. Flux and luminosity have been corrected accounting for the Galactic absorption.

the single power law and the frozen power law plus a blackbody. The results of the bootstrapping are reported in the respective tables: we conclude that neither of the two hypotheses can be discarded from our data on a statistical basis.

We note that the BB parameter estimate is not strongly dependent on the definition of the flaring/quiescent intervals. Indeed, the spectral slope measured during the March quiescent intervals I_q is fully consistent with the November data (Table 2). Freezing the power-law parameters to the best fit of the I_q March intervals or to the November observation does not significantly affect the BB spectral analysis results. We also note that a soft flare, with properties similar to the two episodes registered in March, but with slightly lower statistical significance, is possibly present at ~17 ks from the start of the November 6 segment. Including it in the I_f would not significantly modify either the results of the time-resolved spectral analysis, or their interpretation and the following discussion.

4. Discussion

As reported in the previous section, the soft X-ray emission of PSO J0309+27 has been observed varying in two short time intervals following a softer-when-brighter pattern on a timescale $\Delta\tau_{\mathrm{obs}} \simeq \tau_{\mathrm{raise}} + \tau_{\mathrm{fall}} = 1800$ s corresponding to ~250 s rest frame.

Although tens of years of studies showed that blazars exhibit complex spectral variability on a vast range of timescales, to our knowledge, a change so rapid and with these characteristics has never been described in the X-ray emission of an FSRQ. The intra-day variability reported by Bhatta et al. (2018) for 7 FSRQs is smaller in amplitude and different in spectral behavior, being harder when brighter. Fermi-LAT observations of several FSRQs put in evidence γ-ray flux variations on few hundreds of seconds timescale (Ackermann et al. 2016; Shukla & Mannheim 2020); however, the analysis of the long-term observational campaigns in the X-ray bands has never revealed a similar behavior (e.g., Hayashida et al. 2015; Larionov et al. 2020).

A variable BB emission is what is expected in a BC scenario, where the cold jet electrons up-scatter external UV photons to X-ray energies. This mechanism has been proposed as an observational probe of the lepton content of the blazar jets by Begelman & Sikora (1987) and subsequently deeply investigated by several different authors in the literature (e.g., Sikora et al. 1997; Moderski et al. 2004; Georganopoulos et al. 2005; Celotti et al. 2007). Together with the highly relativistic lepton population, responsible for the SSC emission, the jet should be populated by a commensurate number of electrons which are not relativistic in the co-moving frame. Streaming through an external radiation field with a Lorentz factor ~Γ_{bulk}, these cold electrons would up-scatter photons, producing the so-called BC

emission. In the SMBH proximity, where the jet is thought to be launched, the main external photon source is the AD. In particular, the main contribution to BC emission is expected by those disk photons re-emitted by BLR toward the SMBH since they are seen head-on in the jet frame and, therefore, highly blueshifted by a factor $\sim \Gamma_{\text{bulk}}^2$ (Celotti et al. 2007). Given that most of these photons have energies close to the hydrogen Lyα transition and assuming that the jet bulk Lorentz factor is of the order of $\Gamma_{\text{jet}} \sim 10$, the BC emission is expected to take the form of a variable thermal emission in the soft X-ray (Sikora et al. 1997; Celotti et al. 2007).

The expected transient character of the BC emission is due to the presence of local overdensities within the jet, which are launched very close to the central engine and accelerate up to hundreds or thousands of accretion radii (Celotti et al. 2007; Kataoka et al. 2008). Since the high-energy flares observed in blazar jets are thought to be produced by the collision of shells flowing at different velocities, BC emission is expected as a precursor of γ-ray flares (Moderski et al. 2004).

From an observational point of view, in spite of the fact that, in this particular energy band, FSRQ blazars usually show a minimum of beamed radiation, BC emission has never been clearly and conclusively detected. Celotti et al. (2007) invoked BC emission to explain the departure from a simple power law of the X-ray spectrum of GBB1428+217 at $z = 4.72$; Kataoka et al. (2008), de Rosa et al. (2008) and Kammoun et al. (2018) detected $kT \simeq 1$ keV thermal components in the X-ray spectra of the blazars PKS1510–089 ($z = 0.361$), 4C04.42 ($z = 0.965$) and 4C+25.05 ($z = 2.368$), respectively. However, no clear evidence of the expected variability has been observed so far.

4.1. Bulk Comptonization of Broad-line Photons

As said, the main contribution to BC emission is expected by BLR photons (Celotti et al. 2007). In this scenario, the observed blackbody would have a mean energy

$$KT_{\text{BLR,OBS}} = \delta \ \Gamma_{\text{shell}} KT_{\text{Ly}\alpha}, \tag{2}$$

where δ is the Doppler factor at the viewing angle θ_{view}, $\delta = \frac{1}{\Gamma(1 - \beta \cos \theta_{\text{view}})}$. $KT_{\text{Ly}\alpha}$ is the mean energy of blackbody peaking at a Lyα energy, which is $KT_{\text{Ly}\alpha} = \frac{h\nu_{\text{Ly}\alpha}}{2.82}$ (Celotti et al. 2007).

The expected observed luminosity is:

$$L_{\text{BC}} = \frac{4}{3} c\sigma_T U_{\text{BLR}} \Gamma^2 \delta^4 N_e, \tag{3}$$

where N_e is the number of electrons (Moderski et al. 2004) and U_{BLR} is the energy density of the BLR line emission. This latter can be approximated by $U_{\text{BLR}} = \frac{1}{12\pi}$ erg cm^{-3}, uniform in the region within the BLR radius and independent of the disk luminosity and BLR size (Celotti et al. 2007; Ghisellini 2013). This yields

$$L_{\text{BC}} = 7.08 \times 10^{-16} \text{ erg s}^{-1} \Gamma^2 \delta^4 N_e. \tag{4}$$

The present observation of PSO J0309+27 shows two soft flares, 10 ks apart, with similar characteristics. Given the observed $KT_{\text{BB}} = 0.33^{+0.07}_{-0.06}$, on average, the two shells would
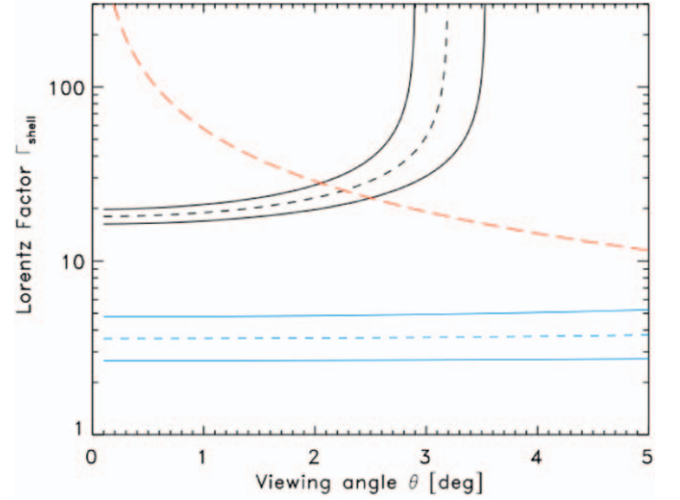

Figure 4. Black lines show the allowed values of the Lorentz factor Γ_{shell} as function of the line-of-sight angle θ_{view}. Blue lines are the values allowed by the core-dominance argument for the Γ_{jet} in the VLBI observation (Spingola et al. 2020). In both cases, dashed lines represent the best values, with continuous lines being the 1σ uncertainties. The red dashed line shows the relation $\Gamma = \frac{1}{\theta_{\text{view}}}$.

have

$$\delta \ \Gamma_{\text{shell}} = \frac{KT_{\text{BB}} \times (1 + z)}{KT_{\text{Ly}\alpha}} = 642^{+136}_{-116}. \tag{5}$$

The region of the Γ-θ_{view} plane satisfying this condition is shown in Figure 4. The constraint on the $\delta \ \Gamma_{\text{shell}}$ product sets an upper limit on the viewing angle $\theta_{\text{view}} \lesssim 3°$. Approaching this limit, the Lorentz factor is constrained to be $\Gamma_{\text{shell}} \gtrsim 20$. With $\theta_{\text{view}} < 2°$, Γ_{shell} is limited to $\sim$20.

In the model presented by Celotti et al. (2007), the flux increase is caused by shell acceleration, with the decline being due to the BLR energy density (U_{BLR}) drop occurring at the limit of the BLR. Unlike this picture, in our data, the observed flare duration $\Delta\tau_{\text{obs}}$ places very tight limits on the size of the emitting region R_X. Indeed, causality requires that $R_X \lesssim c\Delta\tau$, where $\Delta\tau = \Delta\tau_{\text{obs}}\delta\Gamma_{\text{shell}}$ (Ghisellini 2013). Assuming the $\delta\Gamma_{\text{shell}}$ value is constrained by the observed BB energy yields $R_X \sim 10^{16}$ cm equivalent to $\sim$100 gravitational radii, a factor 20 smaller than the estimated size of the BLR of PSO J0309 +27 (see Section 2).

The shape of the observed light curve might be due to the beaming effect of an accelerating shell. In fact, the observed luminosity depends on the factor $\Gamma^2\delta^4$ (Equation (4)). At a given viewing angle θ_{view} (>0), the Doppler factor δ of an increasing Γ_{shell} would peak when $\Gamma_{\text{shell}} \sim \frac{1}{\theta_{\text{view}}}$; at higher value of the Lorentz factor Γ_{shell} the observed emission drops with θ_{view} being larger and larger than $\frac{1}{\Gamma_{\text{shell}}}$ (Ghisellini 2013).

In order to compare data and predictions (Figure 5), we assumed a $\theta_{\text{view}} = 3°$ as required by the Equation (5) condition when $\theta_{\text{view}} \gtrsim \frac{1}{\Gamma_{\text{shell}}}$ (Figure 4) and, for simplicity, a uniformly accelerating shell, which is $\Gamma(x) \propto x$. The predicted light curve is calculated, integrating in the (0.5–2.0) keV band the BB spectrum with the mean energy varying according to Equation (2). We found that a shell accelerating up to $\Gamma_{\text{shell}} \sim 100$ in a space equal to $\sim$100 gravitational radii may match the data, whereas a lower Γ_{shell} maximum value would fail, reproducing the descending slope (Figure 5). A normalization consistent with the observed
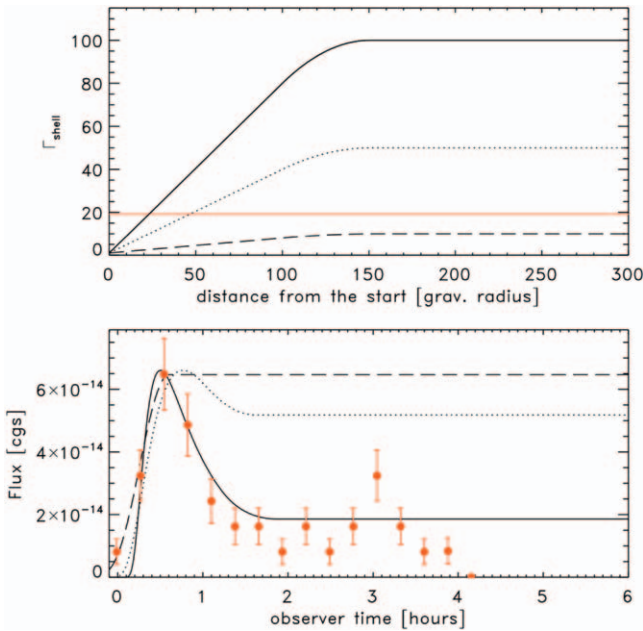
Figure 5. Upper panel: three different shell velocity profiles assumed to compare the prediction of the BLR photons BC model with the observation. In all the cases, the acceleration is uniform up to a maximum value, and from that, the shell is assumed to proceed at constant speed, with $\Gamma_{shell} = 100$, 50, and 10, respectively, reached in a space of $\sim$100 gravitational radii. The red line shows the value $\frac{1}{\theta_{view}}$, assuming $\theta_{view} = 3.0°$. Lower panel: with the assumption of $\theta_{view} = 3.0°$ we show the BC light curve produced in the 0.5–2.0 keV in the three cases with the black continuous, dotted, and dashed lines, respectively, compared to the observed data, shown in red. The light curves have been normalized to match the observed flux and have a maximum when $\Gamma_{shell} \sim \frac{1}{\theta_{view}}$.

flux is provided by $N_e \simeq 5.0 \times 10^{53}$. If we make the assumption that the shell is loaded with the same amount of protons and electrons, this would mean a shell mass $M_{shell} \sim 8 \times 10^{29}$g flowing along the jet in a 160 ks timescale ($\Delta\tau = \Delta\tau_{obs}\delta\Gamma_{shell}$). Given the estimated mass of 8×10^8 solar masses, a luminosity of 0.3 times the Eddington limit (S. Belladitta et al. 2021, in preparation), and assuming a 10% radiative efficiency, this rate would be equivalent to 10%–15% of the SMBH accretion rate. This would mean that, in limited time intervals, a not negligible fraction of the matter usually accreting from the disk onto the SMBH is launched along the jet.

Because the reference model is highly uncertain and we chose it arbitrarily, we limited ourselves to a rough and qualitative comparison, without trying to estimate the best-fit parameters. A physically motivated jet dynamical model, encompassing such an extreme condition is beyond the goal of the present work. Here we just note that a similar shell dynamic has been hypothesized in the case of the FSRQ 3c279 with mass similar to PSO J0309+27 to explain a few hundred seconds of flux variation in the γ-ray ($>$100 MeV) emission (Ackermann et al. 2016).

The shell Lorentz factor value Γ_{shell}, estimated in this context, is significantly higher than the upper limits set by the VLBI data (Spingola et al. 2020) which constrain the Γ_{jet} mean value, between 3–5 as long as $\theta_{obs} \lesssim 4°$ (Figure 4). With Γ_{jet} values at this level, the BC emission would remain confined in the UV band; it becomes observable when faster shells come into action with Lorentz factor values Γ_{shell} high enough to

bring UV photons in the soft X-ray regime and producing spectral variations in observable timescales.

4.2. Bulk Comptonization of Disk Photons

Since the observed flux variation timescale requires that the emission region has to be much smaller than the BLR radius, photons directly coming from the AD might be suitable seeds for the BC. The disk emission is expected to be the superposition of a series of blackbodies with mean energy dependent on the distance from the center according to $r^{-0.75}$ (Shakura & Sunyaev 1973, SS73). Given the mass and the accretion rate of PSO J0309+27 (see Section 2), $KT_{Disk}(r) \lesssim 10$ eV. If involved in the BC process, disk photons should be observed with

$$KT_{obs}(r) = \frac{1 - \beta \ \cos\theta_{disk}}{1 - \beta \ \cos\theta_{view}} KT_{Disk}(r) \qquad (6)$$

where θ_{disk} is the angle between the jet and the directions of the incident photons, with $\theta_{disk} = 0$ when photons and jet have the same direction (Celotti et al. 2007). At small θ_{view} and with high velocities ($\beta \sim 1$), as in the present case, the growth factor could reach values of some hundreds even for $\theta_{disk} < \pi/2$. However, the highest energy photons come from the innermost part of the disk where the θ_{disk} angle is smaller and the energy gain is lower. It follows that cold jet electrons would not be able to up-scatter UV photons to the observed X-ray energies (Figure 6), not even with fast shells like those hypothesized in the previous section.

However, it has been observed that, beside the SS73 disk, many QSOs are characterized by the presence of a hotter component, the so-called X-ray soft excess, with typical mean energies in the 0.1–0.3 keV range (e.g., the case of 3c273, Page et al. 2004) and with luminosities equal to some fraction of the disk ones. The origin of this component is not clear. A popular possibility is that it could be emitted from a comptonizing region lying on the central part of the AD, like a "warm skin," (Janiuk et al. 2001; Done et al. 2012). The IC scattering of these photons by jet cold electrons would explain, at least as a first approximation, both the energy and the timescale of the observed transient emission. In this scenario, in addition to the shell velocity curve, the predictions strongly depend on the geometry of the region responsible for the X-ray soft excess. In Figure 6 we draw a very basic scheme with the only aim of roughly estimating the energies of scattered photons. In this picture, the shell Lorentz factor values, here required, are significantly lower than the ones required by scenario in which the BC is due to the BLR photons.

It is reasonable to think that the same cold electrons responsible for the disk photons' comptonization must subsequently up-scatter the BLR photons as well. However, this would produce an increase of the soft X-ray flux on a timescale of $\sim$2 days, much longer than that in our observation.

4.3. The Case of QSO J074749+115352

Very recently, a few kilosecond timescale variation (3.8 ks) has been marginally detected in the Chandra observation of the QSO J074749+115352 at $z = 5.26$ (Li et al. 2021). Interestingly, this variability follows the same high–soft/low–hard pattern we found for PSO J0309+27, with very similar values of the spectral slopes. If confirmed by statistically better data,
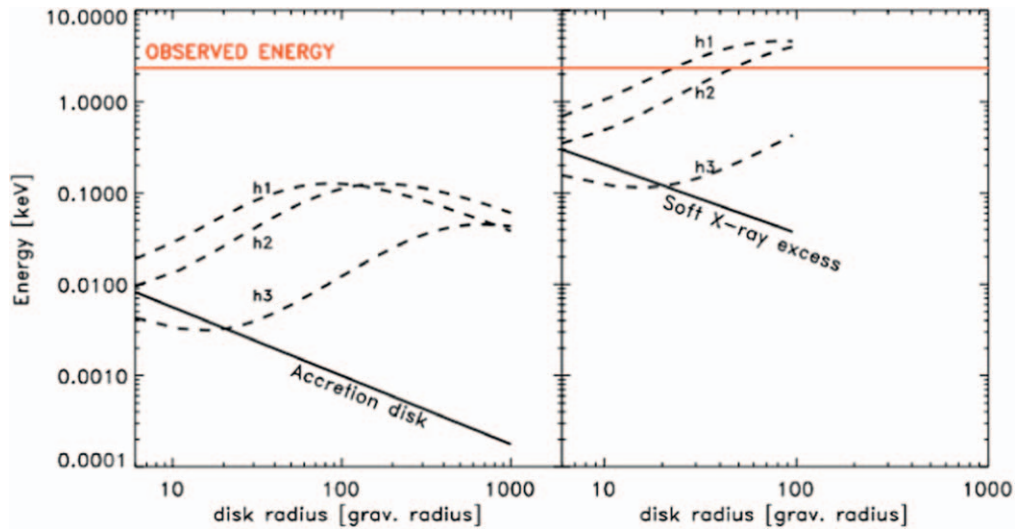
Figure 6. Left panel: the expected temperature profile of the accretion disk (continuous line) and the expected energies after BC at 3 positions in the jet (dashed lines; $h1 = 50$, $h2 = 100$, $h3 = 400$ gravitational radii) , assuming $\Gamma = 20$. Right panel: the same as the left panel, with a temperature profile peaking at 0.3 keV and extending for only 100 gravitational radii in order to naively depict the X-ray soft excess.

the presence of a such a variability in QSO J074749+115352, which is cataloged as a radio-quiet QSO, would possibly undermine our interpretation due to the jet BC emission. However, we note that QSO J074749+115352 is clearly detectable in the VLASS survey (3.0 GHz) at 0.″26 distance from its optical position, with a measured peak flux of 1.76 ± 0.20 mJy corresponding to a luminosity of $\sim 10^{33}$ erg s^{-1}. Since this level of luminosity is typical of radio-loud QSOs, we can conclude that, in the case of QSO J074749+115352 too, the observed emission is likely jet-contaminated.

5. Summary and Conclusions

The two Chandra observations performed 8 months apart point out a significant spectral variation of the emission of the blazar FSRQ PSO J0309+27. This change is entirely due to two soft flares present in the first observation with a similar observed duration of ~ 250 s, rest frame. The extremely short timescale, together with the softer-when-brighter pattern make these events unique in the FSRQ observations reported so far in the literature. The BC of UV external photons by the cold jet electron is a suitable explanation. This process, although never observed, is expected on a theoretical basis as a common feature in the emission produced by leptonic jets. We compared the Chandra dataset with the model predictions. The observed energies are in agreement with the model which predicts that the major contribution to the BC emission is expected by the BLR photons. However, the observed timescale requires an emission region size much smaller than the BLR radius. We found that, in order to roughly reproduce our data, the shell responsible for the BC emission, with BLR photons as seeds, should be accelerated up to $\Gamma_{shell} \sim 100$ on a space scale of $\sim 10^{16}$ cm, equivalent to $\sim$ of 100 gravitational radii.

We also discussed the possibility that the BC seed photons come directly from the AD. This would be consistent with the observed data, if we assume the presence of a soft X-ray excess, as observed in many low-redshift AGNs.

Although not conclusive, the present observations show that the study of the soft X-ray short-timescale variability in FSRQ emission might represent an excellent tool with which to

investigate not only the jet properties but also the innermost QSO environment, which is opaque to higher energies.

ORCID iDs

Alberto Moretti ⓘ https://orcid.org/0000-0002-9770-0315
Gabriele Ghisellini ⓘ https://orcid.org/0000-0002-0037-1974
Alessandro Caccianiga ⓘ https://orcid.org/0000-0002-2339-8264
Silvia Belladitta ⓘ https://orcid.org/0000-0003-4747-4484
Roberto Della Ceca ⓘ https://orcid.org/0000-0001-7551-2252
Tullia Sbarrato ⓘ https://orcid.org/0000-0002-3069-9399
Paola Severgnini ⓘ https://orcid.org/0000-0001-5619-5896
Cristiana Spingola ⓘ https://orcid.org/0000-0002-2231-6861

References

Ackermann, M., Anantua, R., Asano, K., et al. 2016, ApJL, 824, L20
Begelman, M. C., & Sikora, M. 1987, ApJ, 322, 650
Belladitta, S., Moretti, A., Caccianiga, A., et al. 2020, A&A, 635, L7
Bhatta, G., Mohorian, M., & Bilinsky, I. 2018, A&A, 619, A93
Blandford, R., Meier, D., & Readhead, A. 2019, ARA&A, 57, 467
Celotti, A., Ghisellini, G., & Fabian, A. C. 2007, MNRAS, 375, 417
de Rosa, A., Bassani, L., Ubertini, P., Malizia, A., & Dean, A. J. 2008, MNRAS, 388, L54
Done, C., Davis, S. W., Jin, C., Blaes, O., & Ward, M. 2012, MNRAS, 420, 1848
Feigelson, E. D., & Babu, G. J. 2013, in Statistical Methods for Astronomy, ed. T. D. Oswalt & H. E. Bond (Cambridge: Cambridge University Press), 445
Fruscione, A., McDowell, J. C., Allen, G. E., et al. 2006, Proc. SPIE, 6270, 62701V
Georganopoulos, M., Kazanas, D., Perlman, E., & Stecker, F. W. 2005, ApJ, 625, 656
Ghisellini, G. 2013, Radiative Processes in High Energy Astrophysics, Vol. 873 (Berlin: Springer) doi:10.1007/978-3-319-00612-3
Ghisellini, G., & Tavecchio, F. 2009, MNRAS, 397, 985
Giovannini, G., Feretti, L., Venturi, T., et al. 1994, ApJ, 435, 116
Harris, D. E., & Krawczynski, H. 2006, ARA&A, 44, 463
Hayashida, M., Nalewajko, K., Madejski, G. M., et al. 2015, ApJ, 807, 79
Ighina, L., Caccianiga, A., Moretti, A., et al. 2019, MNRAS, 489, 2732
Janiuk, A., Czerny, B., & Madejski, G. M. 2001, ApJ, 557, 408
Kalberla, P. M. W., Burton, W. B., Hartmann, D., et al. 2005, A&A, 440, 775

Kammoun, E. S., Nardini, E., Risaliti, G., et al. 2018, MNRAS, 473, L89
Kataoka, J., Madejski, G., Sikora, M., et al. 2008, ApJ, 672, 787
Larionov, V. M., Jorstad, S. G., Marscher, A. P., et al. 2020, MNRAS, 492, 3829
Li, J.-T., Wang, F., Yang, J., et al. 2021, ApJ, 906, 135
Lira, P., Kaspi, S., Netzer, H., et al. 2018, ApJ, 865, 56
Madejski, G. G., & Sikora, M. 2016, ARA&A, 54, 725
Medvedev, P., Gilfanov, M., Sazonov, S., Schartel, N., & Sunyaev, R. 2021, MNRAS, 504, 576
Moderski, R., Sikora, M., Madejski, G. M., & Kamae, T. 2004, ApJ, 611, 770
Page, K. L., Turner, M. J. L., Done, C., et al. 2004, MNRAS, 349, 57

Press, W. H., Teukolsky, S. A., Vetterling, W. T., & Flannery, B. P. 2002, Numerical Recipes in C++ : the Art of Scientific Computing (Cambridge: Cambridge University Press)
Shakura, N. I., & Sunyaev, R. A. 1973, A&A, 500, 33
Shukla, A., & Mannheim, K. 2020, NatCo, 11, 4176
Sikora, M., Begelman, M. C., Madejski, G. M., & Lasota, J.-P. 2005, ApJ, 625, 72
Sikora, M., & Madejski, G. 2000, ApJ, 534, 109
Sikora, M., Madejski, G., Moderski, R., & Poutanen, J. 1997, ApJ, 484, 108
Spingola, C., Dallacasa, D., Belladitta, S., et al. 2020, A&A, 643, L12
Tavecchio, F., Maraschi, L., Sambruna, R. M., & Urry, C. M. 2000, ApJL, 544, L23